Vicarious spaceborne polarimetric camera calibration using solar power stations

Yannick Bertschy[a] and Yoav Y. Schechner[b]

[a]ETH Zurich, Rämistrasse 101, Zurich, Switzerland
[b]Technion - Israel Institute of Technology, Technion City, Haifa, Israel

ABSTRACT

We propose polarimetric calibration of nano-satellites by pointing them towards solar panel farms or mirrors at solar thermal power plants. We show through simulations that both can provide significant polarization sources. Around a solar tower, this is obtained by polarized skylight reflected from mirrors. Photovoltaic solar panels, on the other hand, yield a strong polarized signal by reflecting direct sunlight around the Brewster angle. The signal is affected by aerosols. The aerosol uncertainty affects calibration tasks. Based on these findings, we simulate spaceborne polarimetric camera calibration.

Keywords: Calibration, Inverse problems, Atmospheric modelling, Polarimetry

1. INTRODUCTION

Optical instruments intended for scientific use should be calibrated. Often, calibration needs to be repeated, or at least validated after some a period of operational use. This need is more significant in spaceborne instruments. An instrument suffers stress during launch and continuous harsh conditions in orbit. These may lead to deviation of the instrument's optical response, despite careful laboratory calibration pre-launch. If the instrument is mounted on a large platform having sufficient resources, in-orbit calibration can be performed using on-board calibration targets. However, spaceborne missions greatly benefit (and even become feasible) by minimization of spacecraft mass, size, and power needs. Limited on-board resources often necessitate exclusion of on-board calibration targets. The alternative is vicarious calibration, using known, distant targets that can be observed by the spaceborne optical payload.

Vicarious methods are already established for calibrating the radiometric and geometric transfer of spaceborne cameras. This paper, however, deals with polarimetric optical sensing. Vicarious polarimetric in-orbit calibration has not received a lot of attention, possibly because space missions carrying scientific polarimetric sensors[1–3] are rarer than those carrying ubiquitous unpolarized optical cameras.

In some science tasks, polarization carries significant information on observed objects. For example, at some ranges of scattering angles, the polarization of light scattered by clouds is sensitive to the cloud particle phase (water, ice) and size parameters. Hence, sensing of polarization can significantly help in retrieval of cloud and aerosol micro-physics.[4–6] This, in turn can solve significant questions in climate research.[6,7] Sensing the microphysics of clouds as 3D volumetric objects is possible using scattering-based computed tomography (CT).[8] Thus, the planned CloudCT space mission, funded by the ERC, is designed to demonstrate polarimetric scattering-based CT of clouds, in order to address climate questions.[9,10] The mission concept is of a large formation of nano-satellites, carrying polarization-sensitive cameras, with no resources to support on-board calibration targets. The ground resolvable distance (GRD) is expected to be about 20-30 meters.

A vicarious polarimetric calibration method requires a known target having degree of linear polarization (DoLP) which is significant and reliable. Uncertainties in the polarization of the target propagate to the calibration product, reducing the scientific value on the mission. Current spaceborne vicarious polarimetric calibration relies on sensing sun-glint, created by reflection by wide water bodies.[7,11] There are two drawbacks to reliance on reflection by open water. First, the polarization signal is affected by the water surface roughness, which partly depends on time-evolving wind and gusts. These environmental conditions often carry significant uncertainty. Second, these methods assume that for any spatial resolvable element in the sensor, the footprint on the water (the GRD) effectively averages contributions of all possible water slopes. This assumption may hold if the GRD

is hundreds of meters wide, effectively integrating spatial periods of typical water waves. This assumption may fail, however, when the GRD is at decameter scale or smaller. This leads to a need for new, alternative vicarious polarimetric calibration principles, which have a smaller calibration uncertainty.

2. THE MAIN IDEA

We propose different calibration targets, whose polarimetric signals are not sensitive to wind and gusts. One possible target is solar-panel farms. A solar panel has a dielectric surface, which can strongly polarize reflected sunlight, mainly near the Brewster angle. Another possible target is a field of solar-tower mirrors. The mirror is metallic, hence not inducing significant polarization by reflection. However, a mirror can reflect the downwelling skylight. Downwelling skylight can be highly polarized, mainly for light propagating in a plane normal to solar irradiance.

The reflected signals in these cases do not depend directly on the wind, contrary to reflection from water. However, the overall signal received at a satellite is still affected by uncertain (yet slowly varying) environmental conditions. Aerosols affect the skylight and sunlight light reaching the targets. Moreover, aerosols affect upwelling atmospheric scattering of sunlight, which also reaches the satellite camera. Thus, there is a need to assess how much uncertainty may be induced by these conditions. Furthermore, there is a need to assess how this uncertainty compares to errors induced by noise inherent to imaging by an optical camera.

3. POLARIMETRIC CALIBRATION

At the top of the atmosphere (TOA), a satellite stares down on Earth. The observed scene radiates to the satellite light which is partially linearly polarized (we neglect circular polarization). This light has unpolarized radiance I_{scene} and a 3-element Stokes vector

$$\boldsymbol{s}_{\text{scene}} = [I_{\text{scene}}, Q_{\text{scene}}, U_{\text{scene}}]^{\top}. \tag{1}$$

The components $Q_{\text{scene}}, U_{\text{scene}}$ depend on an arbitrary coordinate system Ψ.

The satellite has a camera, mounted with a polarization filter (analyzer). The filter has a known angle η in the Ψ coordinate system. The filter has polarizance P. The camera is radiometrically calibrated. When the scene is unpolarized, radiometric calibration relates I_{scene} to the expected camera readout I_{cam}, using a known, calibrated factor c. This factor accounts for the lens aperture, spectral transmissivity, exposure time, quantum efficiency and detector gain and quantization. Generally, the expected camera readout [in photoelectrons] is

$$I_{\text{cam}} = c[I_{\text{scene}} + Q_{\text{scene}} P \cos(2\eta) + U_{\text{scene}} P \sin(2\eta)]. \tag{2}$$

The imaging process is noisy. We suppose the dominant noise source is by photon-noise, modelled with a *Poisson*-distribution. Thus, the actual sampled measured readout is described in

$$I_{\text{cam}}^{\text{measured}} = \text{Poisson}(I_{\text{cam}}). \tag{3}$$

Calibration is based on observing a target (reflector on Earth). The target has an assumed model of Eq. (1) denoted $\boldsymbol{s}_{\text{scene}}^{\text{model}}$, as we describe in Sec. 4. Because the camera is assumed to be radiometrically calibrated, we focus on estimation of P. We provide an example, where a set of L measurements are taken via the same filter. Per measurement $l = 1, ..., L$, the filter is at angle η_l.

Calibration of Polarizance

Using Eq. (2), the assumed model scene $\boldsymbol{s}_{\text{scene}}^{\text{model}}$ yields

$$I_{\text{cam}}^{\text{model}}(P, \eta_l) = c[I_{\text{scene}}^{\text{model}} + Q_{\text{scene}}^{\text{model}} P \cos(2\eta_l) + U_{\text{scene}}^{\text{model}} P \sin(2\eta_l)]. \tag{4}$$

On the other hand, we have noisy measurements $\{I_{\text{cam}}^{\text{measured}}(l)\}_{l=1}^{L}$. In the real world, $\{I_{\text{cam}}^{\text{measured}}(l)\}_{l=1}^{L}$ is a dataset sampled from the camera, without a model. In our study here, $\{I_{\text{cam}}^{\text{measured}}(l)\}_{l=1}^{L}$ are simulated by applying Eq. (2) on $\boldsymbol{s}_{\text{scene}}^{\text{model}}$, using true polarizance P^{true}, and then applying Eq. (3).

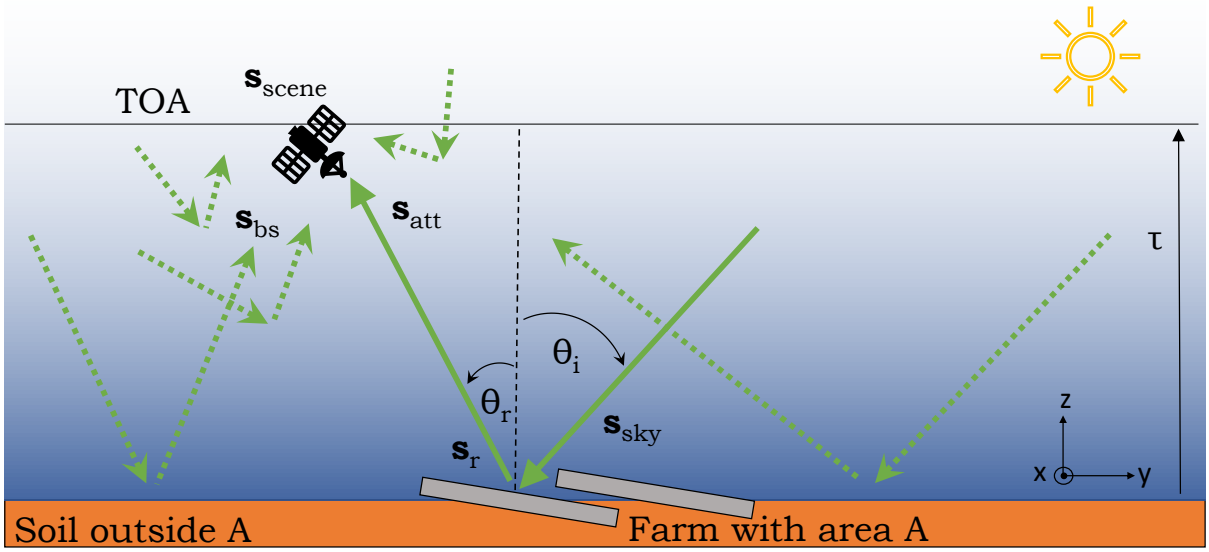

Figure 1: Illustration of the atmosphere and modelling of the Stokes vectors.

Suppose a spaceborne polarimetric sensor uses known angles $\{\eta_l\}_{l=1}^{L}$. However, due to the harsh conditions in orbit, the polarizance drifts from the value that had been determined in the lab. Define a cost function

$$\Gamma(P) = \sum_{l=1}^{L} \left| I_{\text{cam}}^{\text{measured}}(l) - I_{\text{cam}}^{\text{model}}(P, \eta_l) \right|^2 . \tag{5}$$

Then, calibration of P can formulated by a one-dimensional optimization problem

$$\hat{P} = \underset{P}{\operatorname{argmin}}\, \Gamma(P). \tag{6}$$

4. A MODEL FOR THE TARGET SIGNAL

We now derive an approximate model for $\boldsymbol{s}_{\text{scene}}$ of Eq. (1). Consider Fig. 1. A field of mirrors or photovoltaic panels is in area $\mathcal{A}$. Points in the atmosphere have direct lines of sight to any location of the ground: the region around the field (excluding $\mathcal{A}$), is much larger than the area of $\mathcal{A}$. Sunlight irradiates the TOA. Through radiative transfer, this light downwells to the ground. The ground is irradiated by skylight, whose Stokes vector is $\boldsymbol{s}_{\text{sky}}$. It includes both attenuated sunlight and light scattered by the atmosphere. Moreover, through radiative transfer, light is back-scattered to space by the atmosphere, yielding a Stokes vector $\boldsymbol{s}_{\text{bs}}$. This component accounts for upwelling of light due to pure sunlight-atmospheric interactions. The vector $\boldsymbol{s}_{\text{bs}}$ also includes upwelling of scattered light that involves diffuse reflection by the ground, excluding $\mathcal{A}$. In this work, we assume the solar farm region $\mathcal{A}$ is small enough, so that $\boldsymbol{s}_{\text{bs}}$ is not affected by the farm.

The contribution of the solar farm/station is modelled here as reflection of $\boldsymbol{s}_{\text{sky}}$. This reflection includes specular reflection by panels or mirror elements. The reflection also includes diffuse reflection by soil which surrounds each of the elements in the farm. Overall, the reflection is expressed by a Mueller matrix $\boldsymbol{M}_{\text{reflect}}$, which we describe below. The reflected light has Stokes vector

$$\boldsymbol{s}_{\text{r}} = \boldsymbol{M}_{\text{reflect}} \boldsymbol{s}_{\text{sky}}. \tag{7}$$

This light then propagates to the TOA, en route to a satellite. This propagation involves extinction, according to the optical depth τ of the atmosphere. Let θ_{r} be the zenith angle of reflected light heading to the satellite. Then, the attenuated Stokes vector at the TOA is approximately modelled by

$$\boldsymbol{s}_{\text{att}} = \boldsymbol{s}_{\text{r}} \cdot \exp\left(\frac{-\tau}{\cos\theta_{\text{r}}} \right). \tag{8}$$

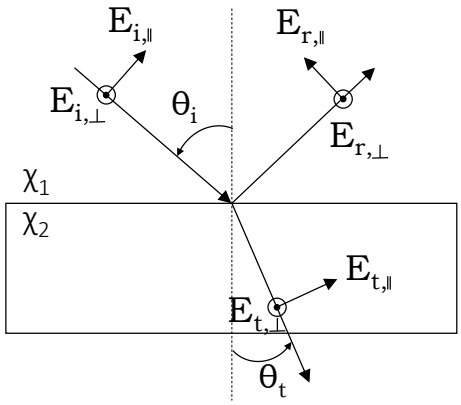

Figure 2: Reflection and transmission at an interface.

This approximation does not account for the spherical curvature of the Earth and its atmosphere, hence it becomes less valid as θ_r grows. From the additive property of Stokes vectors,[12] a combined Stokes vector at the TOA can be described by

$$\boldsymbol{s}_\mathrm{scene} = \boldsymbol{s}_\mathrm{att} + \boldsymbol{s}_\mathrm{bs}, \tag{9}$$

where $\boldsymbol{s}_\mathrm{att}$ is provided in Eq. (8).

4.1 Reflection

We now describe reflection. There are several coordinate systems involved. Because specular reflection is dominant in our case, we start with coordinates aligned with the specular plane of incidence: they constitute the *reflection coordinate system*. Relative to the surface normal, the incidence angle is represented by θ_i. Light partially transmits into the solar panel or mirror by refraction at angle θ_t, relative to the normal (Fig. 2). A medium has a complex[13] reflective index $\hat{\chi} = \chi(1+i\kappa)$, where $i = \sqrt{-1}$. For a dielectric medium, as glass, $\kappa = 0$. The Fresnel reflection coefficients for complex-amplitudes, parallel and perpendicular to the specular plane of incidence are,[14] respectively,

$$R_\parallel = \frac{\hat{\chi}_2 \cos\theta_\mathrm{i} - \hat{\chi}_1 \cos\theta_\mathrm{t}}{\hat{\chi}_2 \cos\theta_\mathrm{i} + \hat{\chi}_1 \cos\theta_\mathrm{t}} \equiv |R_\parallel| \exp(i\delta_\parallel), \qquad R_\perp = \frac{\hat{\chi}_1 \cos\theta_\mathrm{i} - \hat{\chi}_2 \cos\theta_\mathrm{t}}{\hat{\chi}_1 \cos\theta_\mathrm{i} + \hat{\chi}_2 \cos\theta_\mathrm{t}} \equiv |R_\perp| \exp(i\delta_\perp). \tag{10}$$

Define[15]

$$g = \frac{1}{2}(\|R_\parallel^2\| + \|R_\perp^2\|), \qquad \tan(\zeta_1) = \frac{|R_\parallel|}{|R_\perp|}, \qquad \zeta_2 = \delta_\parallel - \delta_\perp. \tag{11}$$

Then define

$$p_1 = 1, \quad p_2 = -\cos(2\zeta_1), \quad p_3 = \sin(2\zeta_1)\cos\zeta_2. \tag{12}$$

We neglect circular polarization, hence use Stokes vectors having three elements. Specular reflection is characterized by 3×3 Mueller matrix.[14] Using the definitions of Eqs. (10,11,12), this matrix is

$$\boldsymbol{M}_\mathrm{spec} = g \begin{bmatrix} p_1 & p_2 & 0 \\ p_2 & p_1 & 0 \\ 0 & 0 & p_3 \end{bmatrix}. \tag{13}$$

Solar panels and mirrors can be imperfect, including scratches or dust. Reflection then is not only specular, but also partly diffuse. Diffuse reflection is also expected from the ground surrounding solar panels or mirrors. This ground has a surface albedo ϖ_surface. The diffuse reflection is assumed here to be Lambertian, which depolarizes light.[16] The Mueller matrix for reflection by a depolarizing Lambertian surface[17] is

$$\boldsymbol{M}_\mathrm{lamb} = \varpi_\mathrm{surface} \cos\theta_\mathrm{i} \begin{bmatrix} 1 & 0 & 0 \\ 0 & 0 & 0 \\ 0 & 0 & 0 \end{bmatrix}, \tag{14}$$

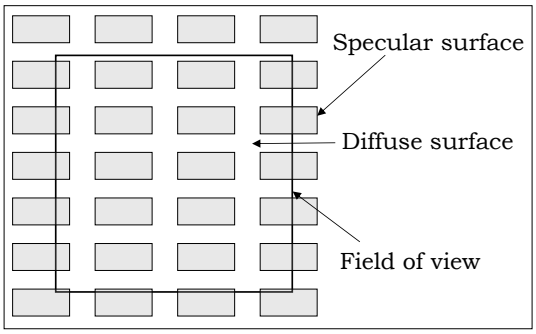

Figure 3: Instantaneous field of view (IFOV) of a pixel observing the ground. The IFOV includes multiple specular reflectors surrounded by a diffuse surface.

where ϖ_{surface} is the surface albedo.

Figure 3 shows the instantaneous field of view (IFOV) of a satellite's pixel. Multiple reflectors are within the field of view and are surrounded by a diffuse surface (e.g. desert). Assume the IFOV is large enough, such that it cannot resolve the specular vs. diffuse regions. Let a_{spec} be the relative weight of specular reflection within the IFOV of a satellite's pixel. Then,

$$a_{\text{lamb}} = 1 - a_{\text{spec}} \tag{15}$$

is the relative weight of diffuse reflection, including the those by surrounding soil and imperfections of the specular surface. Then, reflection is defined by the Mueller matrix

$$\tilde{\boldsymbol{M}}_{\text{reflect}} = a_{\text{spec}} \boldsymbol{M}_{\text{spec}} + a_{\text{lamb}} \boldsymbol{M}_{\text{lamb}}. \tag{16}$$

4.2 Rotation

Equation (16) is valid for the *reflection coordinate system*. However, additional coordinate systems are at play in the signal model. For example scattering, which creates $\boldsymbol{s}_{\text{bs}}$, is more conveniently expressed in a *scattering coordinate system*, defined by the solar radiation direction $\boldsymbol{n}^{\text{i}}$ and the line of sight, $\boldsymbol{n}^{\text{r}}$. To be consistent with common radiative transfer codes, we express $\boldsymbol{s}_{\text{sky}}$ and $\boldsymbol{s}_{\text{bs}}$ in the *meridian coordinate system*. This system is defined by $\boldsymbol{n}^{\text{i}}$ and the zenith direction $\boldsymbol{z}$ at the Earth location being observed. Reflection and scattering events are transferred to the *meridian coordinate system*.

Two rotations are defined between the meridian and the reflection coordinate systems.[18] They involve two angles, measured counter-clockwise,

$$\begin{aligned} \sigma_1 &= \arccos[(\boldsymbol{n}^{\text{i}} \times \boldsymbol{z}) \cdot (\boldsymbol{n}^{\text{i}} \times \boldsymbol{n}^{\text{r}})], \\ \sigma_2 &= \arccos[(\boldsymbol{n}^{\text{r}} \times \boldsymbol{z}) \cdot (\boldsymbol{n}^{\text{r}} \times \boldsymbol{n}^{\text{i}})]. \end{aligned} \tag{17}$$

The rotation angles σ_1 and σ_2 with the incoming and reflected directions of light are depicted in Fig. 4.

A Mueller matrix[19] for rotating a coordinate system by angle σ is

$$\boldsymbol{M}_{\text{rot}}(\sigma) = \begin{bmatrix} 1 & 0 & 0 \\ 0 & \cos(2\sigma) & \sin(2\sigma) \\ 0 & -\sin(2\sigma) & \cos(2\sigma) \end{bmatrix}. \tag{18}$$

Rotating the coordinate system from meridian (where $\boldsymbol{s}_{\text{sky}}$ is often calculated) to the reflection system, and then back[18] to meridian (where the additive $\boldsymbol{s}_{\text{bs}}$ is often calculated) yields the overall rotation matrix

$$\boldsymbol{M}_{\text{reflect}} = \boldsymbol{M}_{\text{rot}}(\sigma_2) \tilde{\boldsymbol{M}}_{\text{reflect}} \boldsymbol{M}_{\text{rot}}(\sigma_1). \tag{19}$$

This is the matrix that we use in Eq. (7). Consequently, $\boldsymbol{s}_{\text{scene}}$ of Eq. (9) is expressed in the *meridian coordinate system*. Thus, we set Ψ in Sec. 3 in this system as well.

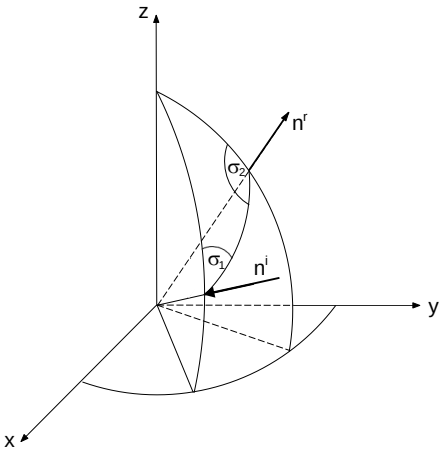

Figure 4: Incoming $\boldsymbol{n}^i$ and reflected directions $\boldsymbol{n}^r$ in a world coordinate system (x, y, z).

4.3 Media

We now describe a few simple models for the reflecting media and atmospheric scatterers. *Solar panels* in a photovoltaic solar *farm* are modeled as uncoated dielectric glass surfaces. The glass refractive index is $\chi_2 = 1.5$. On the other hand, in a solar *thermal power station* light is reflected to a solar *tower*, by mirrors. Mirrors are modeled as smooth aluminium surfaces. The refractive index of aluminium $\hat{\chi_2}$ is complex-valued and wavelength-dependent. For $\lambda = 550$nm, the refractive index[20] of aluminium is $\hat{\chi_2} = 1.0152 + i6.6273$. The refractive index of air is set to $\chi_1 = 1.0$.

Scattering of light by the atmosphere, including scattered light that had been reflected by the ground surrounding $\mathcal{A}$ is modelled by *libRadtran*. This is a library of atmospheric radiative transfer routines that solves the one-dimensional (1D) radiative transfer equations. It simulates an atmosphere including molecules and aerosol particles from standard aerosol models implemented in *libRadtran*. The aerosol models *Continental average*, *Continental polluted* and *Desert* were considered. We made use of the *Monte Carlo code for the phYSically correct Tracing of photons In Cloudy atmospheres*, (*MYSTIC*). This stochastic method was developed as a forward tracing method for the calculation of irradiance and radiance in plane-parallel atmospheres.[18]

The input to *libRadtran* is solar radiation at the TOA. *LibRadtran* outputs downwelling light, $\boldsymbol{s}_{\text{sky}}$ excluding direct sunlight on the ground. The direct sunlight is attenuated by the atmosphere on its path to the ground. This component is calculated separately: it is a Stokes vector denoted $\boldsymbol{s}_{\text{sun}}$, propagating from direction having zenith angle θ_{sun} and azimuth ϕ_{sun}. Then, $\boldsymbol{s}_{\text{sun}}$ is added to $\boldsymbol{s}_{\text{sky}}$:

$$\boldsymbol{s}_{\text{sky}} \leftarrow \boldsymbol{s}_{\text{sky}} + \boldsymbol{s}_{\text{sun}}. \tag{20}$$

5. SIMULATED MODEL SIGNALS

The target signal model was applied to simulate reflection from aluminium mirrors installed around a solar thermal power tower and solar panels simplified by a glass surface. The considered wavelength is $\lambda = 550$nm. The signal depends on the downward viewing direction. So, it is calculated for a hemisphere of downward views. For each viewing direction, the component of Stokes vector $\boldsymbol{s}_{\text{r}}$ are I_{r}, Q_{r} and U_{r}. Analogously, the component of Stokes vector $\boldsymbol{s}_{\text{scene}}$ are I_{scene}, Q_{scene} and U_{scene}. The degree of linear polarization (DoP) of each of these Stokes vectors is respectively

$$\text{DoP}_{\text{r}} = \frac{\sqrt{Q_{\text{r}}^2 + U_{\text{r}}^2}}{I_{\text{r}}}, \qquad \text{DoP}_{\text{scene}} = \frac{\sqrt{Q_{\text{scene}}^2 + U_{\text{scene}}^2}}{I_{\text{scene}}}. \tag{21}$$

In the polar plots below, the nadir is at the origin and the horizon is represented by the outermost circle. The off-nadir angle and azimuth angle are measured radially and tangentially, respectively.

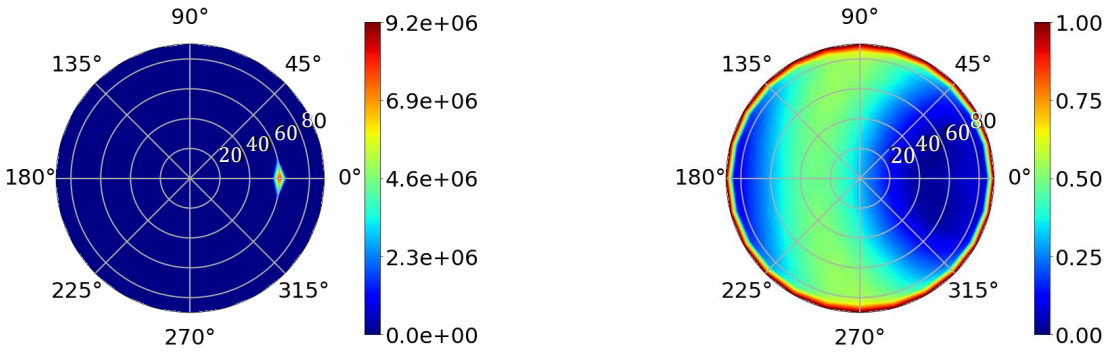

(a) (b)

Figure 5: Combined skylight $\boldsymbol{s}_{\text{scene}}$, measured at the TOA. (a) I_{scene}. (b) $\text{DoP}_{\text{scene}}$.

5.1 Reflection from Aluminium Mirrors

First, consider reflection from aluminium mirrors. The sun direction has zenith and azimuth angles $\theta_{\text{sun}} = 60°$ and $\phi_{\text{sun}} = 0°$. The surface albedo surrounding the mirrors (within $\mathcal{A}$) and the power station as a whole (i.e., the surface excluding $\mathcal{A}$) has $\varpi_{\text{surface}} = 0.05$. Figure 5 shows I_{scene} and $\text{DoP}_{\text{scene}}$ at the TOA, when the aerosol type is *Continental average*.

At first sight, it appears that the target has a favorable $\text{DoP}_{\text{scene}}$, at a wide breadth. This is due to strong polarization of both the skylight (being reflected) and backscatttered light, 90° from the sun. However, we need to consider how sensitive the result is to changes of the aerosol. We considered $\text{DoP}_{\text{scene}}$, for each aerosol type in the three-member set *Continental average*, *Continental polluted* and *Desert*. These are shown in Fig. 6(a,b,c). Then, for each viewing direction, we calculated the standard deviation σ_{DoP} across all three values of $\text{DoP}_{\text{scene}}$. This is displayed in Fig. 6(d). It appears, from this very preliminary and crude test, that in viewing directions of high $\text{DoP}_{\text{scene}}$, the value σ_{DoP} is 0.1 and higher. This means that the results are dominated by aerosols, which are a significant variable in the atmosphere. Hence, if the aerosol environment is not known well during a session of vicarious spaceborne calibration, the calibration of the camera polarizance P may have significant uncertainty. Consequently, there may be a need for another target, which has a lower variability of the DoP.

5.2 Reflection from Solar Panels

We considered reflection from glass solar panels. Here the sun direction has zenith direction corresponding to the Brewster angle, $\theta_{\text{sun}} = 56°$. We set $\phi_{\text{sun}} = 0°$. The surface surrounding the solar panels (within $\mathcal{A}$) and farm (ground excluding$\mathcal{A}$) is sand, having $\varpi_{\text{surface}} = 0.30$. Figure 7 shows I_{scene} and $\text{DoP}_{\text{scene}}$ at the TOA, when the aerosol type is *Desert*.

In most viewing angles, the reflected skylight has rather low intensity, generally, which may inhibit the use of this target. Actually, a ring of strong DoP_{r} exists for all viewing directions at and around the Brewster angle, for all azimuth values. However, notice that such a ring does not exist in Figure 7. The reason is that generally, I_{att} (the intensity of the reflected light, attenuated on the way to the TOA) is much smaller than the backscatter intensity. In other words, the backscatter of the atmosphere overwhelms the signal of the solar panels. The condition of having *both* a high I_{att} *and* high $\text{DoP}_{\text{scene}}$ *simultaneously* is attained when the viewing direction is that of specular-reflection of the sun on the glass surface, at the Brewster angle. So, we focus on this case.

Here too we consider how sensitive the result is to changes of the aerosol, when observing the specular reflection of sunlight at the Brewster angle. We considered $\text{DoP}_{\text{scene}}$, for each aerosol type in the three-member set *Continental average*, *Continental polluted* and *Desert*. They are shown in Tab. 1. The values are slightly lower than 1, despite being at the Brewster angle, because of $\boldsymbol{s}_{\text{bs}}$. The standard deviation σ_{DoP} across the three values of $\text{DoP}_{\text{scene}}$ is also given in Tab. 1. It can be seen that in this viewing direction, $\text{DoP}_{\text{scene}}$ is very high, yet insensitive to the aerosol type.

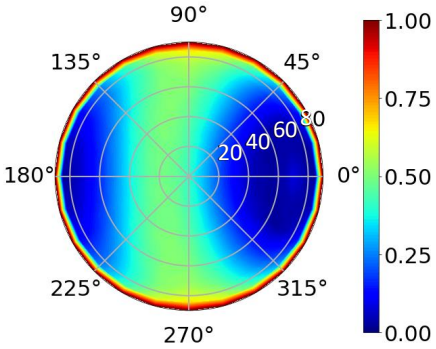

(a)

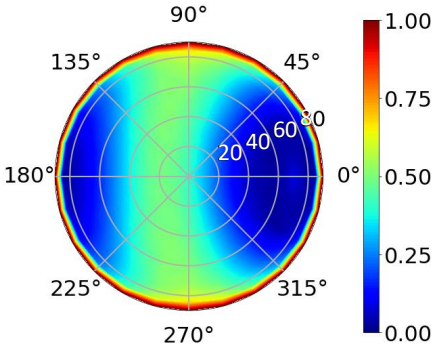

(b)

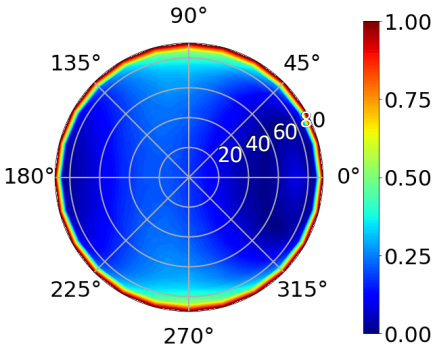

(c)

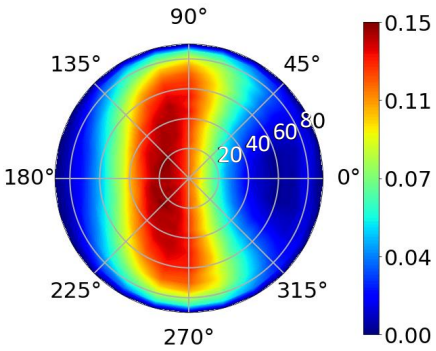

(d)

Figure 6: $\mathrm{DoP}_{\mathrm{scene}}$ for wavelength $\lambda = 550$nm. (a) *Continental average*. (b) *Continental polluted*. (c) *Desert*. (d) Standard deviation σ_{DoP}.

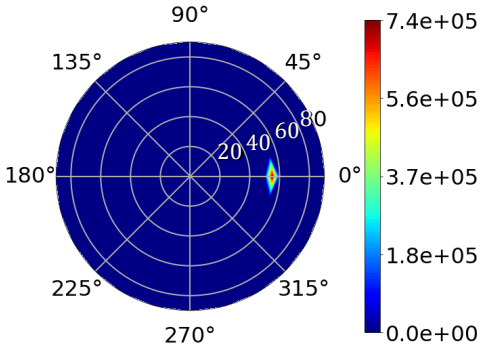

(a)

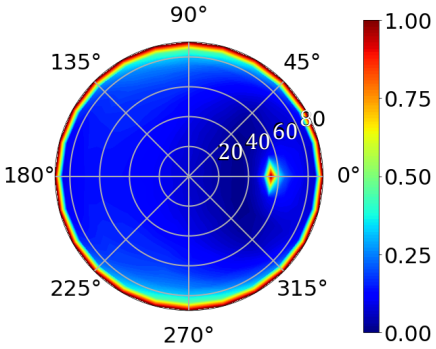

(b)

Figure 7: Combined skylight $\boldsymbol{s}_{\mathrm{scene}}$. (a) I_{scene}. (b) $\mathrm{DoP}_{\mathrm{scene}}$.

6. EXAMPLES OF POLARIMETRIC CALIBRATION

We give an example of polarimetric calibration using horizontal glass surfaces, as described in Sec. 5.2. In the example, $L = 4$ and $\eta_{\mathrm{rel}} = 45°$. Recall Sec. 3. The true value of the polarizance is $0.9 \leq P^{\mathrm{true}} \leq 1$. For each P^{true}, image intensities are simulated as in the model of this paper. The simulated measured data include random photon noise. Then estimation of the polarizance $\hat{P}$ is obtained using Eqs. (5,6). To assess the effect of photon noise, this process is repeated 1000 times, yielding 1000 corresponding estimated values of $\hat{P}$, per P^{true}. Figure 8 plots the estimated polarizance $\hat{P}$ vs. the true polarizance P^{true} for a desert. Furthermore, we investigate the influence of uncertainties in aerosols. Near-site instruments such as a sunphotomoter and/or

Wavelength [nm]	Aerosol Type	$\mathrm{DoP}_{\mathrm{scene}}$	Std. Dev
550	Continental average	0.99986	$3.03 \cdot 10^{-10}$
	Continental polluted	0.99986	
	Desert	0.99986	

Table 1: $\mathrm{DoP}_{\mathrm{scene}}$ at the TOA for different aerosol types. The standard deviation σ_{DoP} is calculated for wavelength $\lambda = 550$nm.

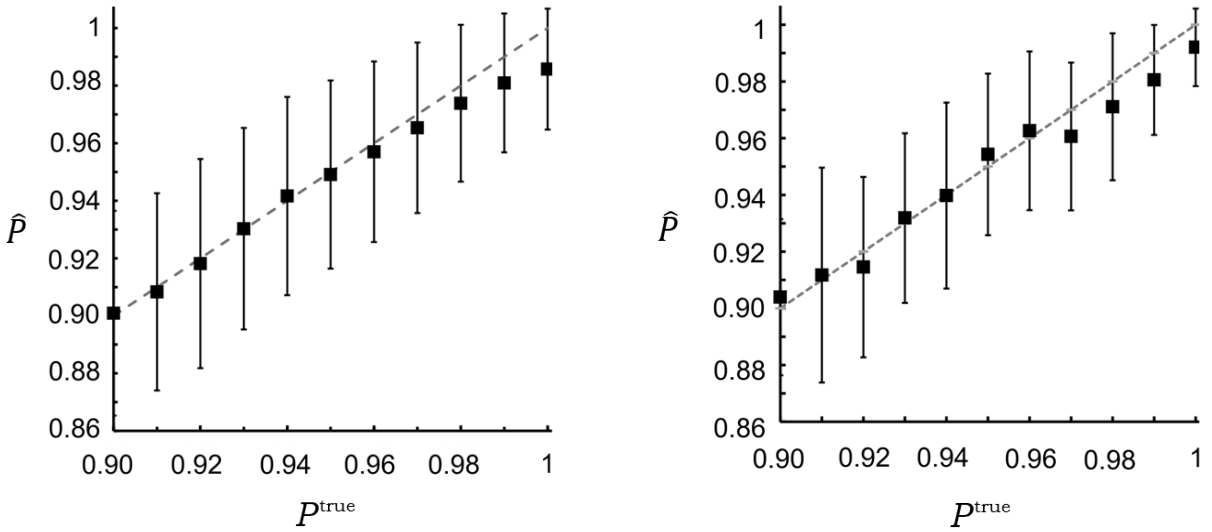

(a) (b)

Figure 8: $\hat{P}$ compared to P^{true} for an aerosol type above a desert. (a) The uncertainty of $\hat{P}$ stems from photon noise. (b) The uncertainty of $\hat{P}$ stems from photon noise and uncertainty in the aerosol density.

aerosol lidar measure the aerosols in the region. However, typical aerosol concentration uncertainties[21] have a standard deviation of $\pm 20\%$. We express this uncertainty by sampling 30 aerosol concentrations from a normal distribution having 20% standard deviation around the settings of the *Desert* aerosol type in *librtran*. The results appear in Figure 8.

7. CONCLUSIONS

At some viewing angles, both types of targets have a strong DoP and can potentially serve for vicarious calibration. However, one may expect uncertainty of the aerosol types and optical depth on-site. This uncertainty affects the calibration, and needs to be considered. This initial work indicates that sunlight reflected from photovoltaic solar panels (approximated by glass) at the Brewster angle is a favorable target for calibration, despite uncertainty of aerosols. Further study is required for the following points: reduction of aerosol uncertainty; on-site estimation of soil properties and diffuse reflection; use in other kinds of polarimetric calibration tasks and use of spherical or 3D (not planar) atmospheric modeling. Of course, we hope that the main idea and principles of this paper will be used in actual calibration of spaceborne sensors.

ACKNOWLEDGMENTS

We thank Joseph Shaw, Vadim Holdovsky and and Masada Tzabari for useful discussions. We thank Johanan Erez, Ina Talmon and Daniel Yagodin for technical support. Yoav Schechner is the Mark and Diane Seiden Chair in Science at the Technion. He is a Landau Fellow - supported by the Taub Foundation. His work is conducted in the Ollendor Minerva Center. Minvera is funded through the BMBF. This research is funded by the European Research Council (ERC) under the European Unions Horizon 2020 research and innovation program (grant agreement No 810370: CloudCT).

REFERENCES

[1] Marbach, T., Fougnie, B., Lacan, A., and Schlüssel, P., "Vicarious calibration of the multiviewing channel polarisation imager (3mi) of the eumetsat polar system-second generation (eps-sg)," in [*Sensors, Systems, and Next-Generation Satellites XX*], **10000**, 294–302, SPIE (2016).

[2] Dubovik, O., Li, Z., Mishchenko, M. I., Tanre, D., Karol, Y., Bojkov, B., Cairns, B., Diner, D. J., Espinosa, W. R., Goloub, P., et al., "Polarimetric remote sensing of atmospheric aerosols: Instruments, methodologies, results, and perspectives," *Journal of Quantitative Spectroscopy and Radiative Transfer* **224**, 474–511 (2019).

[3] Hagolle, O., Goloub, P., Deschamps, P.-Y., Cosnefroy, H., Briottet, X., Bailleul, T., Nicolas, J.-M., Parol, F., Lafrance, B., and Herman, M., "Results of polder in-flight calibration," *IEEE transactions on geoscience and remote sensing* **37**(3), 1550–1566 (1999).

[4] Martins, J. V., Fernandez-Borda, R., McBride, B., Remer, L., and Barbosa, H. M., "The harp hype ran gular imaging polarimeter and the need for small satellite payloads with high science payoff for earth science remote sensing," in [*IGARSS 2018-2018 IEEE International Geoscience and Remote Sensing Symposium*], 6304–6307, IEEE (2018).

[5] Li, Z., Hou, W., Hong, J., Zheng, F., Luo, D., Wang, J., Gu, X., and Qiao, Y., "Directional polarimetric camera (dpc): Monitoring aerosol spectral optical properties over land from satellite observation," *Journal of Quantitative Spectroscopy and Radiative Transfer* **218**, 21–37 (2018).

[6] Sinclair, K., Van Diedenhoven, B., Cairns, B., Alexandrov, M., Moore, R., Crosbie, E., and Ziemba, L., "Polarimetric retrievals of cloud droplet number concentrations," *Remote Sensing of Environment* **228**, 227–240 (2019).

[7] Goloub, P., Toubbe, B., Herman, M., Bailleul, T., Hagolle, O., Martinuzzi, J.-M., and Rouge, B., "In-flight polarization calibration of polder," in [*Advanced and Next-Generation Satellites II*], **2957**, 299–310, SPIE (1997).

[8] Levis, A., Schechner, Y. Y., and Davis, A. B., "Multiple-scattering microphysics tomography," in [*Proceedings of the IEEE Conference on Computer Vision and Pattern Recognition*], 6740–6749 (2017).

[9] K. Schilling, Y. Schechner, I. K., "Cloudct computed tomography of clouds by a small satellite formation," in [*Proceedings 12th IAA symposium on Small Satellites for Earth Observation*], IFAC (2019).

[10] K. Schilling, Y. Schechner, I. K., "Cloudct: A formation of cooperating nano-satellites for cloud characterisation by computed tomography," in [*Proceedings 70th International Astronautical Congress 2019, IAC-19 D1.6.54792*], (2019).

[11] Guo, J., Yao, Z., Han, Z., Zhao, Z., Jiang, J., and Yan, W., "On-orbit polarization calibration of the multi-angle polarization imager based on sunglint over the ocean," in [*Proceedings of the Tiangong-2 Remote Sensing Application Conference*], 144–159, Springer (2019).

[12] Bohren, C. F. and Huffman, D. R., [*Absorption and scattering of light by small particles*], John Wiley & Sons (2008).

[13] Rouard, P. and Meessen, A., "Ii optical properties of thin metal films," in [*Progress in Optics*], **15**, 77–137, Elsevier (1977).

[14] Wallace, A. M., Liang, B., Trucco, E., and Clark, J., "Improving depth image acquisition using polarized light," *International Journal of Computer Vision* **32**(2), 87–109 (1999).

[15] Born, M. and Wolf, E., [*Principles of optics: electromagnetic theory of propagation, interference and diffraction of light*], CUP Archive (2000).

[16] Chen, H.-S. and Rao, C. N., "Polarization of light on reflection by some natural surfaces," *Journal of Physics D: Applied Physics* **1**(9), 1191 (1968).

[17] Chipman, R. A., "Polarimetry," *Handbook of Optics* **2**, 22–1 (1994).

[18] Emde, C., Buras, R., Mayer, B., and Blumthaler, M., "The impact of aerosols on polarized sky radiance: model development, validation, and applications," *Atmospheric Chemistry and Physics* **10**(2), 383–396 (2010).

[19] Bass, M., DeCusatis, C., Lakshminarayanan, V., Li, G., Macdonald, C., Mahajan, V., Van Stryland, E., and Enoch, J. M., [*Optics: Vol. 1: Geometrical and Physical Optics, Polarized Light, Components and Instruments*], McGraw-Hill Professional Pub. (2009).

[20] Rakić, A. D., "Algorithm for the determination of intrinsic optical constants of metal films: application to aluminum," *Applied optics* **34**(22), 4755–4767 (1995).

[21] Heese, B., Floutsi, A. A., Baars, H., Althausen, D., Hofer, J., Herzog, A., Mewes, S., Radenz, M., and Schechner, Y. Y., "The vertical aerosol type distribution above israel–2 years of lidar observations at the coastal city of haifa," *Atmospheric Chemistry and Physics Discussions* , 1–22 (2021).